

# All-Dielectric Surface-Enhanced Infrared Absorption-Based Gas Sensor Using Guided Resonance

Yuhua Chang,<sup>†,‡</sup> Dihan Hasan,<sup>†,‡</sup> Bowei Dong,<sup>†,‡</sup> Jingxuan Wei,<sup>†,‡</sup> Yiming Ma,<sup>†,‡</sup> Guangya Zhou,<sup>§</sup> Kah Wee Ang,<sup>†</sup> and Chengkuo Lee<sup>\*,†,‡</sup>

<sup>†</sup>Department of Electrical and Computer Engineering, National University of Singapore, 117583, Singapore

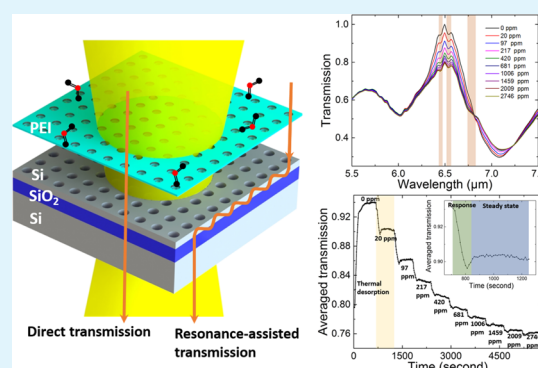
<sup>‡</sup>Center for Intelligent Sensors and MEMS, National University of Singapore, 117608, Singapore

<sup>§</sup>Department of Mechanical Engineering, National University of Singapore, 117575, Singapore

## Supporting Information

**ABSTRACT:** The surface-enhanced infrared absorption (SEIRA) technique has been focusing on the metallic resonator structures for decades, exploring different approaches to enhance sensitivity. Although the high enhancement is achieved, the dissipative loss and strong heating are the intrinsic drawbacks of metals. Recently, the dielectric platform has emerged as a promising alternative. In this work, we report a guided resonance-based all-dielectric photonic crystal slab as the platform for SEIRA. The guided resonance-induced enhancement in the effective path length and electric field, together with gas enrichment polymer coating, leads to a detection limit of 20 ppm in carbon dioxide (CO<sub>2</sub>) sensing. This work explores the feasibility to apply low loss all-dielectric structures as a surface enhancement method in the transmission mode.

**KEYWORDS:** photonic crystal slab, all-dielectric, guided resonance, surface enhanced infrared absorption, gas sensor, gas enrichment polymer



The surface-enhanced infrared absorption (SEIRA) technique has garnered extensive attention over the last decade for its ability to detect molecular fingerprints with monolayer sensitivity on chips.<sup>1,2</sup> Metal-based optical resonators are commonly deployed for enhancing light–matter interactions through strong near-field coupling and thereby artificially enhancing the intrinsic signal of molecules by various mechanisms. Among them, spoof surface plasmon polaritons (SPPs),<sup>3</sup> Fano effect,<sup>4</sup> and Fabry–Pérot mechanism<sup>5</sup> have been extensively studied to exceed the existing detection limit. Various structures, for example, split-ring resonators,<sup>6,7</sup> nanorods,<sup>8,9</sup> nanoslits,<sup>10</sup> bow-ties,<sup>11</sup> and metal–dielectric–metal-based perfect absorbers,<sup>12,13</sup> have been reported to achieve high sensitivity at mid-IR. However, highly multiplexed sensing which requires no spectral overlap is hindered because of resonance with a low quality factor originated from strong damping (radiation and intrinsic) in metals. Besides, the volume of light–matter interaction is limited, leading to inefficient utilization of surrounding analytes because the enhanced near-fields are usually highly localized around the “hot spots” such as at the tips of the nanorods and the nanogaps of bow-ties and split-ring resonators.<sup>14</sup> Meanwhile, transmission mode sensing which is preferred in an integrated sensor system is ineffective because of the metal loss. Furthermore, metals are subject to optical heating for their intrinsic Ohmic losses, making the label-free detection at mid-IR unreliable as the line shapes of various

functional groups are highly temperature dependent. Therefore, an all-dielectric material platform with low loss, large volume of light–matter interactions, and high transmission will show great potentials for integrated chip-level gas sensing.

Recently, all-dielectric nanostructures including the nanodisk and photonic crystal slab (PCS) with a large electric field enhancement have emerged as alternatives for a metal-based platform for highly sensitive sensors. A higher quality (*Q*) factor and weaker heating effect than their metallic counterparts are expected from the low loss of dielectric materials. Although a relatively high *Q* factor can be achieved by a dielectric nanodisk, the mode is quite well-confined inside the structure. Such a feature is ideal for nonlinear wavelength conversion<sup>15,16</sup> but undesirable for the detection of surrounding analytes as the effective light–matter interaction is suppressed by the inaccessibility.<sup>17,18</sup> These refractive index (RI)-based sensors require complicated surface functionalization to enable selectivity. On the contrary, the PCS shows its advantages over the nanodisk in terms of the *Q* factor and mode distribution. A much higher *Q* factor on the order of 10<sup>4</sup> is achieved by slightly tilting the incident beam or creating an alternating nanohole size for a better sensitivity in RI sensing.<sup>19,20</sup> A large portion of the electric field is exposed to

Received: September 24, 2018

Accepted: October 17, 2018

Published: October 17, 2018

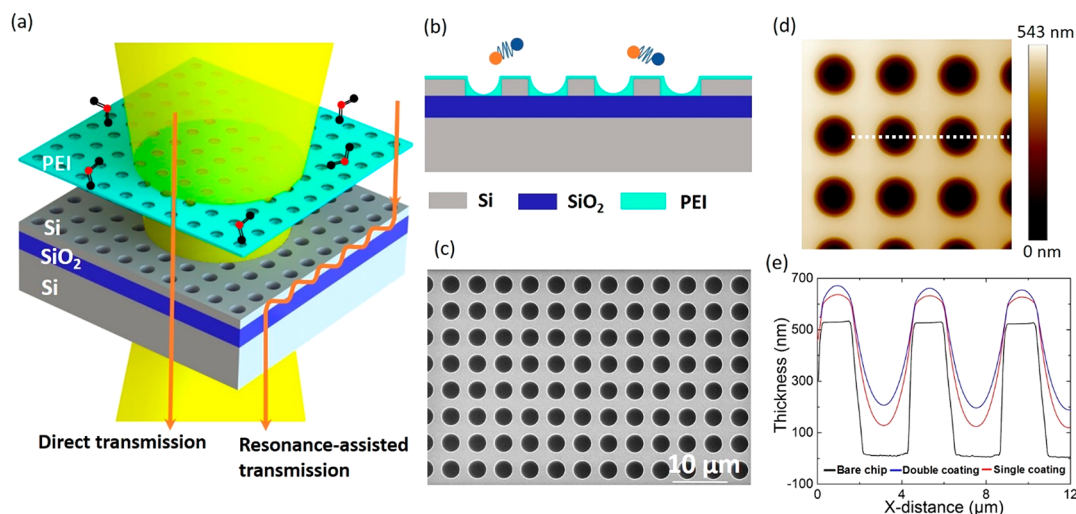


**Figure 1.** (a) Schematic illustration and (b) cross section of the device and the sensing mechanism. (c) SEM image of the PCS before PEI coating. (d) AFM image of the PCS with PEI coating. (e) Surface profiles of the PCS at bare chip, single coating, and double coating along the white dash line in (d).

the surrounding analytes once the TE-like or TM-like mode is excited.<sup>21</sup> With these two advantages, total absorption in the graphene monolayer is studied theoretically by critical coupling,<sup>22,23</sup> and nearly 100% absorption is demonstrated experimentally in near infrared with the PCS integrated with a back reflector.<sup>24</sup> However, the platform still operates in the reflection mode, making it less suitable for integrated gas sensors.

Gas sensors with a miniaturized size, ultrahigh sensitivity, and fast response time still remain as a challenge for small size and weak absorption of gas molecules. To tackle this problem, various two-dimensional materials like graphene,<sup>25–30</sup> black phosphorus,<sup>31–33</sup> and MoS<sub>2</sub><sup>34,35</sup> have been investigated for the on-chip gas sensor, demonstrating an ultrahigh detection limit and ultrafast response time for NO, N<sub>2</sub>O, NH<sub>3</sub>, and CO<sub>2</sub>. However, the selectivity requires further efforts such as pattern recognition<sup>36</sup> and doping.<sup>37,38</sup> Another solution is to deploy a gas selective enrichment layer such as the metal–organic framework (MOF) to locally enhance the gas concentration and exploit the near-field enhancement from metamaterial patterns.<sup>39–41</sup> Chong et al. engineered the coupled SPP for a better spatial overlap of the electric field with MOF and demonstrated enhanced CO<sub>2</sub> sensing.<sup>42</sup> However, the sensitivity is still limited because the interaction between the tiny CO<sub>2</sub> molecule (232 pm in length) and the plasmonic pattern is weak for detection at the ppm (parts per million) level. The response time is potentially hindered by the 2.7 μm thick MOF.<sup>40</sup> In an alternative scheme of the hybrid metamaterial absorber, we reported sensitivity down to 40 ppm by utilizing the molecular vibrations at mid-IR, which originates from the transformation of chemical compositions in the gas-selective polymer polyethylenimine (PEI). However, the metallic structure reported is still subject to intrinsic loss and heating and can only operate in the reflection mode.<sup>13</sup> In this work, we demonstrate an all-dielectric SEIRA-based PCS platform operating in the transmission mode for CO<sub>2</sub> sensing. Two mechanisms induced by guided resonance in the PCS are identified to enhance gas selective absorption in PEI, that is, the uniformly enhanced electric field and the enlarged effective path length. The experimental results indicate 14 times enhancement of the absorption signal on the PCS structure

as compared to the unpatterned thin film. A detection limit of 20 ppm with a response time of 2 min is achieved on a significantly miniaturized gas sensor platform (array size 220 μm × 220 μm).

## RESULTS AND DISCUSSION

**Guided Resonance and Its Near-Field Coupling.** The device and the sensing mechanism are shown schematically in Figure 1a,b. The PCS is fabricated from the silicon-on-insulator (SOI) wafer with 1 μm buried oxide (BOX) and a 500 nm device layer. The periodic index contrast on the silicon slab creates phase matching conditions, through which external radiation can be coupled into the slab and excites guided resonance. The light resonates inside the slab during its lifetime and then leaks back to free space. The constructive interference occurs between this resonance-assisted transmission and direct transmission, giving rise to an enhanced electric field in the near-field and transmission peak in the far field.<sup>43,44</sup> The incident light is an unpolarized light cone with an angle up to 45°. The scanning electron microscopy (SEM) image of the fabricated PCS is shown in Figure 1c. PEI is an amine-based polymer that can absorb and react with CO<sub>2</sub> selectively.<sup>45</sup> The vibration and stretching of some molecules after the absorption of CO<sub>2</sub> result into the significant fingerprints from 6.06 to 7.69 μm (see the Supporting Information for related chemical reactions). A thicker PEI film can absorb more CO<sub>2</sub>, increasing the detection range but at the expense of the response time. Single coating of PEI on SOI at 4000 rpm is found to be around 125 nm thick (Figure S1a). An atomic force microscopy (AFM) image in Figure 1d shows a surface roughness of 2.5 nm. To achieve a thicker PEI layer, coating twice is preferred because high viscosity will lead to nonuniformity if the spin speed is low. Figure 1e is the surface profile along the white dash line in Figure 1d. Double coating leads to a minor thickness increase of around 30 nm (Figure S1b) on the Si surface and a better filling inside the air holes, that is, a stronger interaction between PEI and the electric field.

Major parameters for the PCS design are the radius to period ( $r/a$ ) ratio and thickness of the BOX layer and the Si device layer. The transmission spectrum as a function of the  $r/$

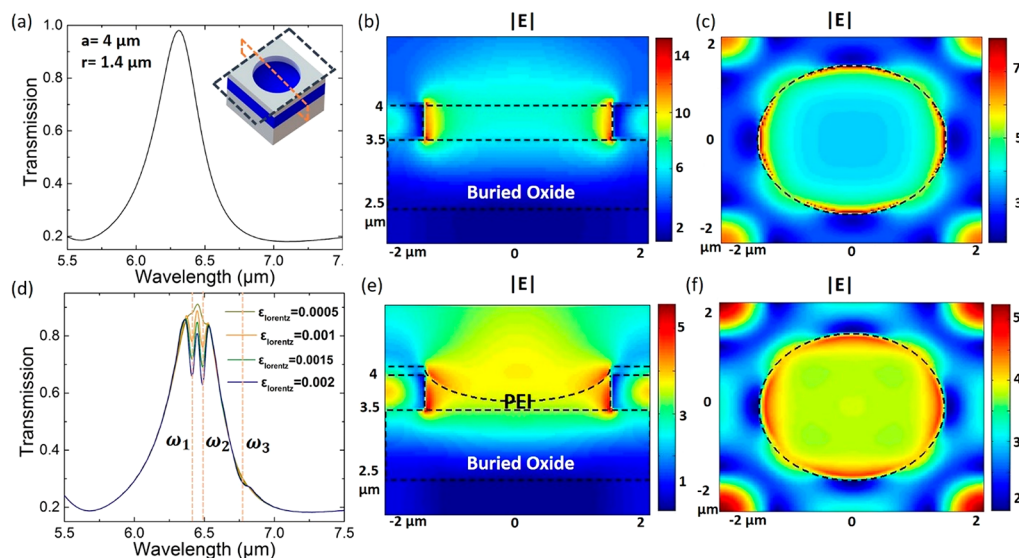


**Figure 2.** (a) Simulated transmission spectrum of the normally illuminated PCS. The inset is a unit cell of the PCS where the orange line cuts through the mid, and the black line is at the Si-air interface. E-field distributions at the resonance peak at these two planes are shown in (b) cross section and (c) top view. (d) Simulated spectrum of the normally illuminated PCS after a layer of absorption material is added. Different coupling strengths are to simulate the different CO<sub>2</sub> concentrations. (e) Cross-sectional and (f) top view of E field distribution at  $\omega_1$ .

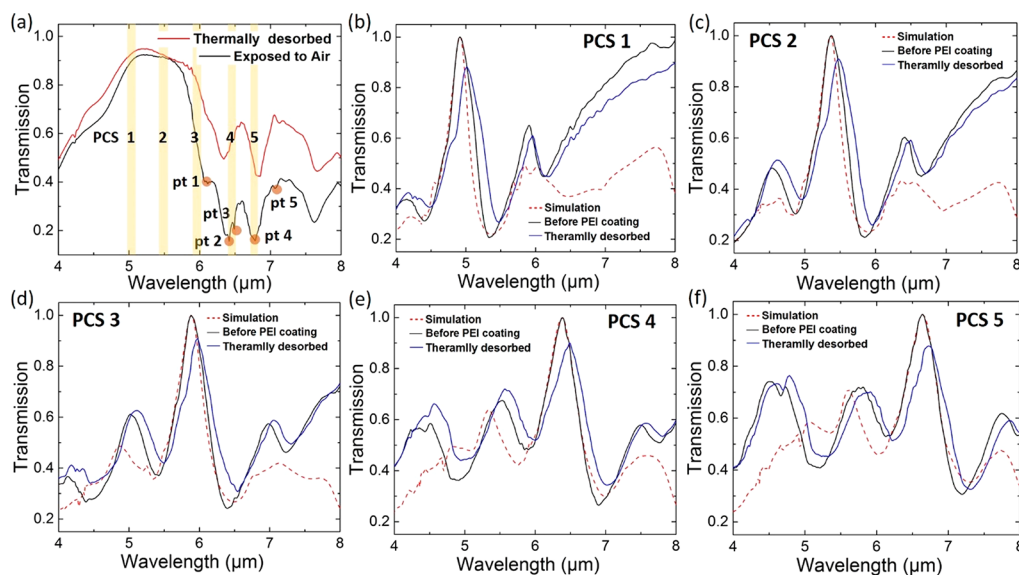


**Figure 3.** (a) Typical transmission spectrum of a several microns thick PEI film in the air environment and at the thermally desorbed state. Five points at 6.073, 6.416, 6.490, 6.786, and 7.064  $\mu\text{m}$  are circled to characterize the near-field coupling. Pt 1 is the N-H deformation peak. Pt 2, 3 are from the stretching of C=O and pt 4, 5 are from the vibration of NCOO. The shaded area shows the peak positions of PCS 1-5. (b-f) Simulated spectrum (under the illumination of the light cone: red dashed line) and the measured spectrum (before PEI coating: black line; thermally desorbed state: blue line) of PCS 1-5.

$a$  ratio is shown in Figure S2a. A larger  $r/a$  ratio scatters more light and decreases resonance lifetime and quality factor, while more electric field can penetrate into the air hole.<sup>21</sup> The transmission intensity also increases. Figure S2b shows a periodic behavior between transmission and BOX thickness, indicating that the BOX spacing layer works as a phase shifter that determines the interference condition between the directly transmitted beam and the resonance-assisted beam. The effects of Si device layer thickness are studied as shown in Figure S2c. Although complicated resonance behaviors happen at short wavelength, major resonance at longer wavelength is red-shifted almost linearly with the increased Si slab thickness. This shows the importance of the Si layer to support the

resonance.<sup>46</sup> More high-order modes arise when the slab is too thick. The final thicknesses of Si and BOX are determined by the commercially available SOI wafer as 500 nm and 1  $\mu\text{m}$ , respectively. The  $r/a$  ratio is chosen as 0.35 for both high transmission and quality factor.

The simulated spectrum of the PCS (radius  $r = 1.4 \mu\text{m}$ ,  $a = 4 \mu\text{m}$ ,  $r/a = 0.35$ ) is shown in Figure 2a. The cross-sectional view and the top view of the TE-like mode at the resonance peak are shown in Figure 2b,c. The electric field is considerably localized along the Si-air interface at the sidewall. The 500 nm thick device layer compensates the relatively small field enhancement factor from the dielectric structure. The penetration of the electric field into BOX reduces the

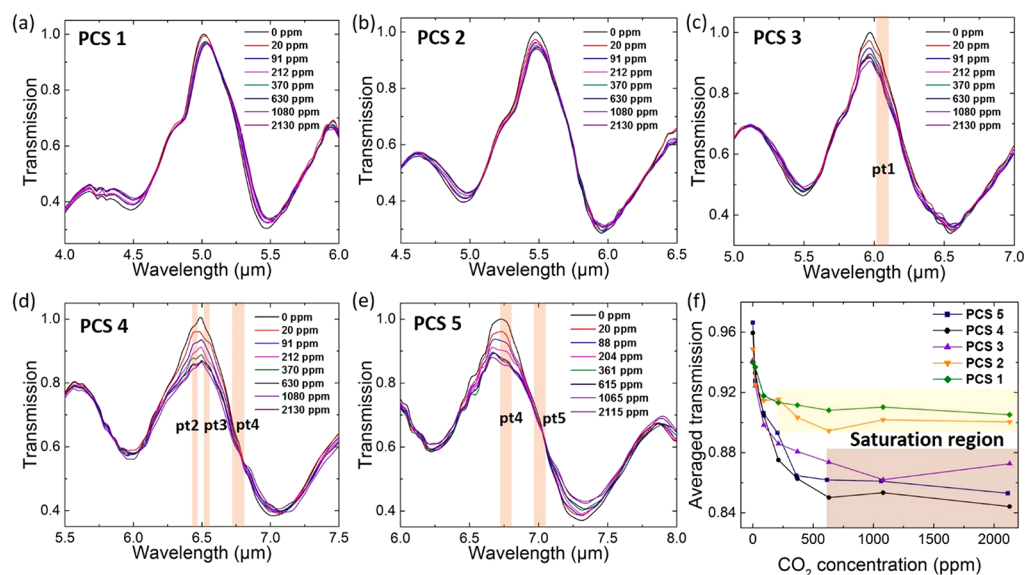


**Figure 4.** (a–e) Transmission spectra of single coated PCS 1–5 at different CO<sub>2</sub> concentrations. Shaded areas correspond to the absorption peaks of PEI marked in Figure 3a. (f) Averaged transmission of PCS 1–5 at different CO<sub>2</sub> concentrations for single PEI coating. Light and dark shaded areas correspond to the saturation region for PCS 1 and 2 and PCS 3, 4, and 5, respectively.

sensitivity. To estimate the absorption effect of PEI when it is exposed to CO<sub>2</sub>, a representative material is defined by the Lorentz model  $\varepsilon = \varepsilon_0 + \sum_{i=1}^3 \varepsilon_{\text{Lorentz}} \omega_i / (\omega_i^2 - 2i\delta_0\omega - \omega^2)$ , where  $\varepsilon_0 = 1.96$  and  $\delta_0 = 8 \times 10^{11}$  rad/s. The oscillator strength  $\varepsilon_{\text{Lorentz}}$  varies from 0.0005 to 0.002. Three center frequencies  $\omega_i$  at 6.416, 6.490, and 6.786  $\mu\text{m}$  are marked by  $\omega_1$ ,  $\omega_2$ , and  $\omega_3$ , respectively. The simulated spectrum at different coupling strengths is depicted in Figure 2d. As compared to Figure 2a, the resonance peak is red-shifted around 100 nm, and a clear electromagnetic-induced transparency-like phenomenon can be observed. The enhancement factor at  $\omega_1$  and  $\omega_2$  is estimated around 260 and 280, whereas  $\omega_3$  is enhanced by 150 times only (Figure S3a). This is because  $\omega_3$  is not perfectly matched with the peak around 6.45  $\mu\text{m}$ , where the resonance strength is maximized and the electric field is highly concentrated. The mode distribution at  $\omega_1$  is shown in Figure 2e,f. As a result of the low RI of the polymer, the evanescent field penetrates further into PEI. The electric field enhancement decreases when compared with Figure 2b because of the extra loss introduced by PEI. To further illustrate the mechanism of the absorption enhancement, simulations are performed with isolated coating layers at different places: top, sidewall, and bottom, as shown in Figure S3b. The absorption-induced dips from the bottom coating layer are more pronounced than those from the top and sidewall coating. However, the electric field is not highly localized at the PEI–SiO<sub>2</sub> interface. On the contrast, although there is a uniformly enhanced electric field along the sidewall, the absorption enhancement is only slightly higher than that at the PCS top, where the strong electric field is exposed at certain spots. Such a phenomenon is attributed to two enhancement mechanisms. First, the enhancement from the bottom is the result of the guided resonance-assisted transmission. The incident wave is coupled into the PCS and then resonates inside with both transmission and reflection occurring at the boundary. Therefore, the path length in the absorption material is effectively enlarged by multiple round trips.<sup>47</sup> Second, guided resonance is also accompanied by the enhanced electric field.

The overall enhancement from the top is improved by a large area, whereas the active area from 500 nm thick sidewall is limited.

**Characterization with Single PEI Coating.** Five PCSs are fabricated with peaks spanning from 4.91 to 6.64  $\mu\text{m}$ . The  $r/a$  ratio are kept the same at 0.355. Their geometrical and key measured parameters are summarized in Table S1. Figure 3a illustrates the transmission spectrum of several microns thick PEI under thermally desorbed states (0 ppm) and in the air environment (around 400 ppm), respectively (see the Method section for detailed characterization steps). Significant differences in transmission spectra can be seen from 6.06 to 7.69  $\mu\text{m}$  because the absorbed species of the carbamate–ammonium pair (1650–1300  $\text{cm}^{-1}$ ) emerge upon the reaction between CO<sub>2</sub> and PEI. Absorption peaks from N–H deformation, C=O stretching, and NCOO skeletal vibration at 6.073, 6.416, 6.490, 6.786, and 7.064  $\mu\text{m}$  are marked by pt 1–5, respectively. Shaded areas indicate the peak positions of five designed PCSs. Figure 3b–f shows the simulated spectrum of PCS 1–5 under the illumination of the light cone (see the Method section for light cone simulation), and the measured spectrum before PEI coating and at the thermally desorbed state. The measured major resonance peaks match simulated results at 4.91, 5.37, 5.88, 6.38, and 6.64  $\mu\text{m}$  in PCS 1–5, respectively. Some minor side peaks are observed besides those major peaks because the PCS spectrum may be changed significantly by the oblique incident light from Fourier transform infrared spectrometer (FTIR), and dark states may be excited.<sup>48,49</sup> The spectra under normal incident light and the light cone are simulated in Figure S4, confirming that the incident angle induces this discrepancy between design and measurement. Compared with spectra before PEI coating, the peaks under the thermally desorbed state are red-shifted around 100 nm. Quality factors, as well as transmission intensity, drop because of the extra loss from PEI.

The transmission spectra of PCS 1–5 at different CO<sub>2</sub> concentrations are shown in Figure 4a–e. The wavelengths corresponding to the five absorption peaks in Figure 3a are also marked for comparison. The spectrum is normalized to the

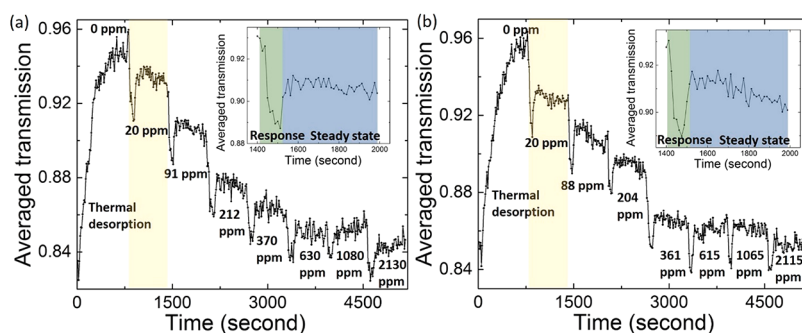


**Figure 5.** Dynamical behavior of (a) PCS 4 and (b) PCS 5 at single PEI coating. The inset is a zoomed-in image of the shaded area, showing a response time of around 2 min.

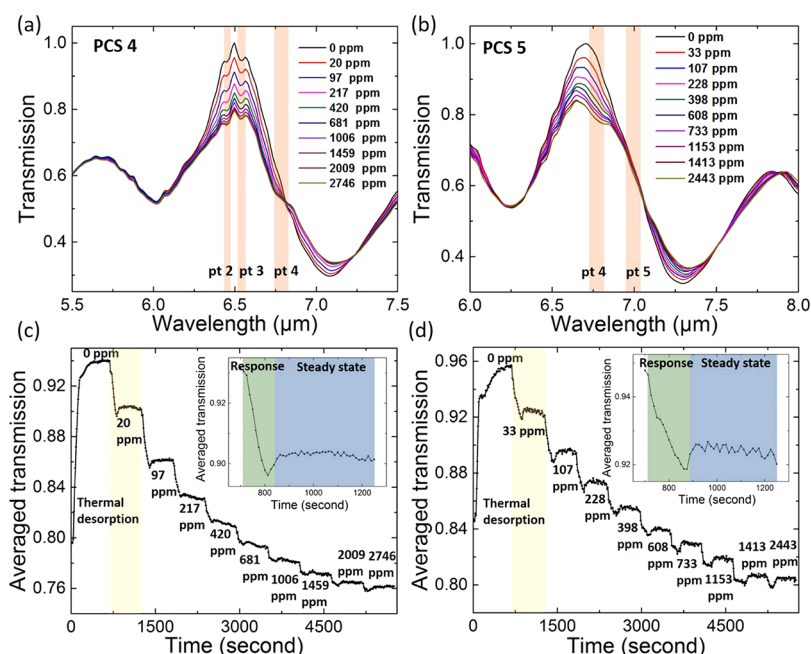


**Figure 6.** Spectrum of double coated (a) PCS 4 and (b) PCS 5 at different CO<sub>2</sub> concentrations. The shaded area corresponds to the absorption peaks of PEI marked in Figure 3a. Dynamical behavior of (c) PCS 4 and (d) PCS 5 at double PEI coating. The inset is a zoomed-in image of the shaded area, showing a slower response around 3 min.

initial thermally desorbed state to show the sensing effect clearly. Peak intensity barely decreases for PCS 1 and 2, and they saturate quickly because these two peaks are far away from the sensing window from 6.06 to 7.69  $\mu\text{m}$ . The calibration emerges at PCS 3 as it approaches pt 1 which is the deformation peak from N–H in  $\text{RNH}_3^+$ . The resonance wavelength of PCS 4 and 5 matches the stretching peak of C=O and the skeletal vibration of NCOO, enabling the most obvious calibration. Slight line shape modification is also observed from absorption dips at pt 1–5. The demonstrated detection limit is 20 ppm, but it still shows the potential to push the limit down to 10 ppm. If such an enrichment layer is applied to a nondispersive infrared system, a band pass filter is required to select the target wavelength range, and only the overall intensity can be detected. Therefore, an averaged transmission is defined as  $T_{\text{avg}} = \frac{1}{\lambda_1 - \lambda_2} \int_{\lambda_2}^{\lambda_1} T(\lambda) d\lambda$  to better illustrate the sensing performance, where  $\lambda_1$  and  $\lambda_2$  are the lower and upper wavelength boundary of the integral (the integral window is shown in Figure S6).<sup>13</sup> The averaged transmission is shown in Figure 4f, where a sensing region is followed by a saturation region. The dynamic range, which is

the transmission difference between the thermally desorbed state and saturation state, keeps increasing from PCS 1 to PCS 5 as resonance peaks of PCS and PEI vibration modes are becoming overlapped. Saturation concentration, representing the detection range, is also extended from 200 to 600 ppm. To quantitatively evaluate the enhancement from the PCS, the sample without the pattern, that is, the SOI chip coated with 125 nm PEI, is measured at an ambient environment and thermally desorbed states, shown in Figure S7a. The enhancement factors are calculated as 12.20 and 14.52 for PCS 4 and 5 (see the Supporting Information for calculation methods), respectively. The degradation of the enhancement factor compared to simulation is mainly because of the quality factor which is reduced by the oblique light cone (Figure S4) and fabrication imperfections such as surface roughness and the sidewall. The reduced quality factor represents a weaker enhancement in the electric field and path length.

The dynamical behavior is analyzed in Figure 5a,b for PCS 4 and 5, which match the sensing window of PEI and thus have a better performance. The transmission keeps increasing during the thermal desorption and finally reaches a steady CO<sub>2</sub>-free state. Then, after each injection of CO<sub>2</sub>, there is a clear

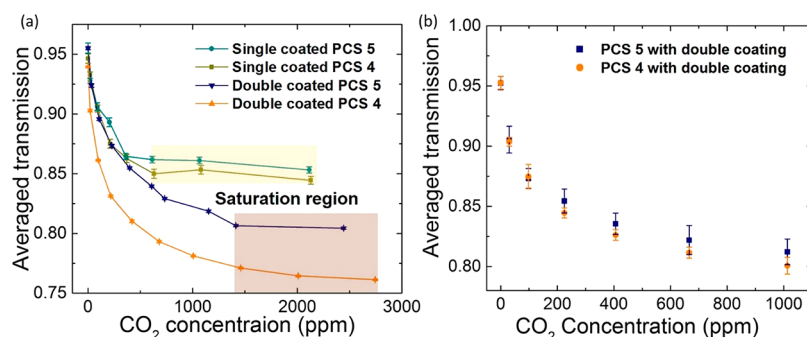


**Figure 7.** (a) Averaged transmission of PCS 4 and 5 at different CO<sub>2</sub> concentrations for both single and double PEI coating. Error bars indicate the standard deviation of 20 continuous measurements on the same pattern. Light and dark shaded areas represent the saturation region for single-coated PCSs and double-coated PCSs, respectively. (b) Averaged transmission of six PCS 4 and six PCS 5. Error bars represent standard deviation among devices.

decrease followed by fluctuation around the same level. Saturation occurs when the CO<sub>2</sub> concentration reaches 600 ppm. The inset is a zoomed-in image of the shaded area about how average transmission evolves from injection to the steady state. The sharp dip immediately after the injection is caused by fast CO<sub>2</sub> absorption occurring on the PEI surface and then slow diffusion into the bulk of PEI. A minor recovery before steady states is resulted from which some of the CO<sub>2</sub> molecules on the surface are driven away by the carrier gas N<sub>2</sub>. The response time from the injection to steady states is estimated around 2 min.

**Characterization with Double PEI Coating.** To investigate the effect of different PEI thicknesses, the double-coated PCS 4 and 5 are characterized after the previous PEI is removed by O<sub>2</sub> plasma. The spectrums at the steady states are presented in Figure 6a,b. A characteristic split is more obvious at pt 2, 3, and 4 in double-coated PCS 4 than that of single coating. Similar results have been shown in Figure 2e by simulation. However, the enhancement of vibration peak resolution at pt 4 in PCS 5 is less pronounced because double coating slightly blue-shifts the peak of PCS 5 from 6.73 to 6.70 μm, whereas the peak of PCS 4 remains unchanged. Considering that two PCSs are on the same chip, this difference in peak shifts is due to imperfections in coating uniformity resulted from high viscosity of PEI. Pt 4 shifts away from the resonance peak of PCS 5, where the enhancement is the strongest. PEI thickness increase is counteracted by the decrease in the PCS enhancement. Therefore, the overall enhancement is moderate. Because the peak position depends on the surrounding effective index, negligible peak shifts (<0.5%) also infer that there is no strong overlap between the second layer of the coated PEI and the evanescent field which will otherwise change the surrounding effective index significantly. The enhanced electric fields along the Si–air sidewall and on top of the PCS have already been almost fully utilized by the first layer of the coated PEI. The improved resolution in vibration modes comes from the elongated light–matter interaction length induced by guided resonance. The response time is slowed down from 2 to 3 min as shown by the inset in Figure 6c,d. As the PEI layer is thicker, CO<sub>2</sub> molecules need to diffuse a longer path to fill the bulk. The enhancement factors are quantitatively calculated as 13.30 for PCS 4 and 12.78 for PCS 5 by comparing with the unpatterned sample, whose spectrum is in Figure S7b.

Averaged transmissions for the double-coated PCS 4 and 5 are calculated in Figure 7a by the same method as mentioned

above. Averaged transmissions for single-coated counterparts are also shown for comparison. The error bar represents the standard deviation of 20 continuous measurements under the same CO<sub>2</sub> concentrations. Error bars for the double-coated PCS are smaller than those for the single-coated PCS, which indicate that more volume of bulk PEI is available for CO<sub>2</sub> to diffuse into, so that absorbed CO<sub>2</sub> is less affected by the gas flow on the surface. The detection range is extended from 600 to 1400 ppm, whereas PEI thickness is increased by only 30 nm (Figure S1) by double coating, confirming the remarkable enhancement. The sensitivity around 100 ppm for these four samples is estimated as 0.0394%/ppm (PCS 4, single coating), 0.0317%/ppm (PCS 5, single coating), 0.0537%/ppm (PCS 4, double coating), and 0.0381%/ppm (PCS 5, double coating) (see Figure S8 for sensitivity). The increase in coating thickness affects the dynamic range and the detection range more than sensitivity. The device reliability test is performed (devices image in Figure S9) by measuring six identical PCS 4 and PCS 5. The standard deviation among devices is presented in Figure 7b, which is caused mainly by the imperfections in coating uniformity.

In summary, we demonstrate an all-dielectric SEIRA-based PCS integrated with CO<sub>2</sub>-selective enrichment polymer PEI for CO<sub>2</sub> sensing using the transmission mode. Unlike metal-based SEIRA where the electric field is highly localized around the hot spots, the enhancement of PCS is the result of two mechanisms induced by guided resonance, that is, the enlarged effective path length due to multiple round trips inside the slab and the uniformly enhanced electric field along the sidewall. Boosted by the selective enrichment and chemical reactions from the 125 nm thin PEI film, as well as 14 times enhancement from the PCS pattern, the CO<sub>2</sub> sensor is demonstrated to have a detection limit of 20 ppm with a fast response time of 2 min. A thicker PEI coating layer increases the detection range and dynamic range at the expense of the response time. This work explores the promising possibilities of the photonic crystal as the surface-enhanced structure for sensing applications.

## METHOD

**Nanofabrication.** PCSs are fabricated on an SOI wafer (500 nm top silicon, 1 μm BOX, 725 μm handle wafer), using electron beam lithography and deep reactive ion etching. Then, a thin layer of 125 nm thick PEI (diluted in deionized water with a mass ratio of 1:10) is spin-coated on the PCS at a speed of 4000 rpm.

**Numerical Simulation.** The simulation is performed by FDTD (Lumerical Inc). Periodic boundary conditions and perfect matching layers are applied to the unit cell. The spectrums of both s-wave and p-wave at varying incident angles from 0° to 45° are weighted and summed incoherently to simulate the unpolarized light cone. The Broadband Fixed Angle Source Technique (BFAST) is involved as the light source.

**Infrared Spectrum Characterization.** The infrared spectrums of PCS are characterized by a Fourier transformed infrared microscope (Agilent Cary 610 Series) from 4 to 8  $\mu\text{m}$ , with a gas chamber and heating stage placed at the light path. The PEI-coated PCS is first flushed by  $\text{N}_2$  at 70 C until steady state to fully desorb  $\text{CO}_2$  from the ambient environment. Then,  $\text{CO}_2$  sensing is performed at room temperature, 30% humidity, and the continuous mode, that is, no thermal reset between two  $\text{CO}_2$  concentrations. The  $\text{CO}_2$  concentration is calibrated by a commercial  $\text{CO}_2$  meter. Both inlet and outlet are kept open during the continuous injection of gas. During the dynamic mode, FTIR is set to get a data point for each 12.5 s. The measured spectrum is normalized to an SOI sample.

## ■ ASSOCIATED CONTENT

### 📄 Supporting Information

The Supporting Information is available free of charge on the ACS Publications website at DOI: 10.1021/acsami.8b16623.

PEI characterization, numerical simulation of the PCS, experiment setup and PCS characterization, enhancement calculation, sensitivity calculation, and device reliability test (PDF)

## ■ AUTHOR INFORMATION

### Corresponding Author

\*E-mail: [elelc@nus.edu.sg](mailto:elelc@nus.edu.sg)

### ORCID

Yuhua Chang: 0000-0003-0337-1934

Kah Wee Ang: 0000-0003-1919-3351

Chengkuo Lee: 0000-0002-8886-3649

### Notes

The authors declare no competing financial interest.

## ■ ACKNOWLEDGMENTS

This work is sponsored by NRF-CRP15-2015-02 “Piezoelectric Photonics Using CMOS Compatible AlN Technology for Enabling the Next Generation Photonics ICs and Nanosensors” (WBS: R-263-000-C24-281) at NUS, Singapore and “Hybrid Integration of Flexible Power Source and Pressure Sensors” (R-263-501-012-133) at NUS.

## ■ REFERENCES

- (1) Hartstein, A.; Kirtley, J. R.; Tsang, J. C. Enhancement of the infrared absorption from molecular monolayers with thin metal overlayers. *Phys. Rev. Lett.* **1980**, *45*, 201–204.
- (2) Neubrech, F.; Huck, C.; Weber, K.; Pucci, A.; Giessen, H. Surface-enhanced infrared spectroscopy using resonant nanoantennas. *Chem. Rev.* **2017**, *117*, 5110–5145.
- (3) Ng, B.; Hanham, S. M.; Wu, J.; Fernández-Domínguez, A. I.; Klein, N.; Liew, Y. F.; Breese, M. B. H.; Hong, M.; Maier, S. A. Broadband terahertz sensing on spoof plasmon surfaces. *ACS Photonics* **2014**, *1*, 1059–1067.
- (4) Wu, C.; Khanikaev, A. B.; Adato, R.; Arju, N.; Yanik, A. A.; Altug, H.; Shvets, G. Fano-resonant asymmetric metamaterials for

ultrasensitive spectroscopy and identification of molecular monolayers. *Nat. Mater.* **2012**, *11*, 69–75.

(5) Brown, L. V.; Yang, X.; Zhao, K.; Zheng, B. Y.; Nordlander, P.; Halas, N. J. Fan-shaped gold nanoantennas above reflective substrates for surface-enhanced infrared absorption (SEIRA). *Nano Lett.* **2015**, *15*, 1272–1280.

(6) Lahiri, B.; Khokhar, A. Z.; De La Rue, R. M.; McMeekin, S. G.; Johnson, N. P. Asymmetric split ring resonators for optical sensing of organic materials. *Optic Express* **2009**, *17*, 1107–1115.

(7) Cubukcu, E.; Zhang, S.; Park, Y.-S.; Bartal, G.; Zhang, X. Split ring resonator sensors for infrared detection of single molecular monolayers. *Appl. Phys. Lett.* **2009**, *95*, 043113.

(8) Neubrech, F.; Kolb, T.; Lovrincic, R.; Fahsold, G.; Pucci, A.; Aizpurua, J.; Cornelius, T. W.; Toimil-Molares, M. E.; Neumann, R.; Karim, S. Resonances of individual metal nanowires in the infrared. *Appl. Phys. Lett.* **2006**, *89*, 253104.

(9) Neubrech, F.; Pucci, A.; Cornelius, T. W.; Karim, S.; García-Etxarri, A.; Aizpurua, J. Resonant plasmonic and vibrational coupling in a tailored nanoantenna for infrared detection. *Phys. Rev. Lett.* **2008**, *101*, 157403.

(10) Huck, C.; Vogt, J.; Sendner, M.; Hengstler, D.; Neubrech, F.; Pucci, A. Plasmonic enhancement of infrared vibrational signals: nanoslits versus nanorods. *ACS Photonics* **2015**, *2*, 1489–1497.

(11) Hasan, D.; Lee, C. A modified abstraction of Sierpiński fractals towards enhanced sensitivity of a cross-coupled bow-tie nanostructure. *Nano Futures* **2018**, *2*, 025005.

(12) Chen, K.; Adato, R.; Altug, H. Dual-band perfect absorber for multispectral plasmon-enhanced infrared spectroscopy. *ACS Nano* **2012**, *6*, 7998–8006.

(13) Hasan, D.; Lee, C. Hybrid Metamaterial Absorber Platform for Sensing of  $\text{CO}_2$  Gas at Mid-IR. *Adv. Sci.* **2018**, *5*, 1700581.

(14) Neuman, T.; Alonso-González, P.; García-Etxarri, A.; Schnell, M.; Hillenbrand, R.; Aizpurua, J. Mapping the near fields of plasmonic nanoantennas by scattering-type scanning near-field optical microscopy. *Laser Photon. Rev.* **2015**, *9*, 637–649.

(15) Grinblat, G.; Li, Y.; Nielsen, M. P.; Oulton, R. F.; Maier, S. A. Efficient third harmonic generation and nonlinear subwavelength imaging at a higher-order anapole mode in a single germanium nanodisk. *ACS Nano* **2016**, *11*, 953–960.

(16) Grinblat, G.; Li, Y.; Nielsen, M. P.; Oulton, R. F.; Maier, S. A. Degenerate four-wave mixing in a multiresonant germanium nanodisk. *ACS Photonics* **2017**, *4*, 2144–2149.

(17) Bontempi, N.; Chong, K. E.; Orton, H. W.; Staude, I.; Choi, D.-Y.; Alessandri, I.; Kivshar, Y. S.; Neshev, D. N. Highly sensitive biosensors based on all-dielectric nanoresonators. *Nanoscale* **2017**, *9*, 4972–4980.

(18) Yavas, O.; Svedendahl, M.; Dobosz, P.; Sanz, V.; Quidant, R. On-a-chip biosensing based on all-dielectric nanoresonators. *Nano Lett.* **2017**, *17*, 4421–4426.

(19) Liu, Y.; Wang, S.; Zhao, D.; Zhou, W.; Sun, Y. High quality factor photonic crystal filter at  $k \approx 0$  and its application for refractive index sensing. *Opt. Express* **2017**, *25*, 10536–10545.

(20) Nicolaou, C.; Lau, W. T.; Gad, R.; Akhavan, H.; Schilling, R.; Levi, O. Enhanced detection limit by dark mode perturbation in 2D photonic crystal slab refractive index sensors. *Optic Express* **2013**, *21*, 31698–31712.

(21) El Beheiry, M.; Liu, V.; Fan, S.; Levi, O. Sensitivity enhancement in photonic crystal slab biosensors. *Optic Express* **2010**, *18*, 22702–22714.

(22) Piper, J. R.; Fan, S. Total absorption in a graphene monolayer in the optical regime by critical coupling with a photonic crystal guided resonance. *ACS Photonics* **2014**, *1*, 347–353.

(23) Piper, J. R.; Liu, V.; Fan, S. Total absorption by degenerate critical coupling. *Appl. Phys. Lett.* **2014**, *104*, 251110.

(24) Liu, Y.; Chadha, A.; Zhao, D.; Piper, J. R.; Jia, Y.; Shuai, Y.; Menon, L.; Yang, H.; Ma, Z.; Fan, S.; Xia, F.; Zhou, W. Approaching total absorption at near infrared in a large area monolayer graphene by critical coupling. *Appl. Phys. Lett.* **2014**, *105*, 181105.

- (25) Chen, G.; Paronyan, T. M.; Harutyunyan, A. R. Sub-ppt gas detection with pristine graphene. *Appl. Phys. Lett.* **2012**, *101*, 053119.
- (26) Yoon, H. J.; Jun, D. H.; Yang, J. H.; Zhou, Z.; Yang, S. S.; Cheng, M. M.-C. Carbon dioxide gas sensor using a graphene sheet. *Sens. Actuators, B* **2011**, *157*, 310–313.
- (27) Zhu, J.; Ruan, B.; You, Q.; Guo, J.; Dai, X.; Xiang, Y. Terahertz imaging sensor based on the strong coupling of surface plasmon polaritons between PVDF and graphene. *Sens. Actuators, B* **2018**, *264*, 398–403.
- (28) Xiang, Y.; Zhu, J.; Wu, L.; You, Q.; Ruan, B.; Dai, X. Highly sensitive terahertz gas sensor based on surface plasmon resonance with graphene. *IEEE Photonics J.* **2018**, *10*, 1–7.
- (29) Varghese, S. S.; Lonkar, S.; Singh, K. K.; Swaminathan, S.; Abdala, A. Recent advances in graphene based gas sensors. *Sens. Actuators, B* **2015**, *218*, 160–183.
- (30) Singh, E.; Meyyappan, M.; Nalwa, H. S. Flexible graphene-based wearable gas and chemical sensors. *ACS Appl. Mater. Interfaces* **2017**, *9*, 34544–34586.
- (31) Wu, L.; Wang, Q.; Ruan, B.; Zhu, J.; You, Q.; Dai, X.; Xiang, Y. High-Performance Lossy-Mode Resonance Sensor Based on Few-Layer Black Phosphorus. *J. Phys. Chem. C* **2018**, *122*, 7368–7373.
- (32) Abbas, A. N.; Liu, B.; Chen, L.; Ma, Y.; Cong, S.; Aroonyadet, N.; Köpf, M.; Nilges, T.; Zhou, C. Black phosphorus gas sensors. *ACS Nano* **2015**, *9*, 5618–5624.
- (33) Cho, S.-Y.; Lee, Y.; Koh, H.-J.; Jung, H.; Kim, J.-S.; Yoo, H.-W.; Kim, J.; Jung, H.-T. Superior Chemical Sensing Performance of Black Phosphorus: Comparison with MoS<sub>2</sub> and Graphene. *Adv. Mater.* **2016**, *28*, 7020–7028.
- (34) He, Q.; Zeng, Z.; Yin, Z.; Li, H.; Wu, S.; Huang, X.; Zhang, H. Fabrication of Flexible MoS<sub>2</sub> Thin-Film Transistor Arrays for Practical Gas-Sensing Applications. *Small* **2012**, *8*, 2994–2999.
- (35) Li, H.; Yin, Z.; He, Q.; Li, H.; Huang, X.; Lu, G.; Fam, D. W. H.; Tok, A. I. Y.; Zhang, Q.; Zhang, H. Fabrication of Single- and Multilayer MoS<sub>2</sub> Film-Based Field-Effect Transistors for Sensing NO at Room Temperature. *Small* **2012**, *8*, 63–67.
- (36) Choi, S.-J.; Kim, S.-J.; Kim, I.-D. Ultrafast optical reduction of graphene oxide sheets on colorless polyimide film for wearable chemical sensors. *NPG Asia Mater.* **2016**, *8*, No. e315.
- (37) Zhang, D.; Liu, J.; Jiang, C.; Liu, A.; Xia, B. Quantitative detection of formaldehyde and ammonia gas via metal oxide-modified graphene-based sensor array combining with neural network model. *Sens. Actuators, B* **2017**, *240*, 55–65.
- (38) Yuan, W.; Huang, L.; Zhou, Q.; Shi, G. Ultrasensitive and selective nitrogen dioxide sensor based on self-assembled graphene/polymer composite nanofibers. *ACS Appl. Mater. Interfaces* **2014**, *6*, 17003–17008.
- (39) Kim, K.-J.; Chong, X.; Kreider, P. B.; Ma, G.; Ohodnicki, P. R.; Baltrus, J. P.; Wang, A. X.; Chang, C.-H. Plasmonics-enhanced metal-organic framework nanoporous films for highly sensitive near-infrared absorption. *J. Mater. Chem. C* **2015**, *3*, 2763–2767.
- (40) Chong, X.; Kim, K.-J.; Li, E.; Zhang, Y.; Ohodnicki, P. R.; Chang, C.-H.; Wang, A. X. Near-infrared absorption gas sensing with metal-organic framework on optical fibers. *Sens. Actuators, B* **2016**, *232*, 43–51.
- (41) Kreno, L. E.; Hupp, J. T.; Van Duyne, R. P. Metal–Organic Framework Thin Film for Enhanced Localized Surface Plasmon Resonance Gas Sensing. *Anal. Chem.* **2010**, *82*, 8042–8046.
- (42) Chong, X.; Zhang, Y.; Li, E.; Kim, K.-J.; Ohodnicki, P. R.; Chang, C.-h.; Wang, A. X. Surface-Enhanced Infrared Absorption: Pushing the Frontier for On-Chip Gas Sensing. *ACS Sens.* **2018**, *3*, 230–238.
- (43) Fan, S.; Joannopoulos, J. D. Analysis of guided resonances in photonic crystal slabs. *Phys. Rev. B: Condens. Matter Mater. Phys.* **2002**, *65*, 235112.
- (44) Zhou, W.; Zhao, D.; Shuai, Y.-C.; Yang, H.; Chuwongin, S.; Chadha, A.; Seo, J.-H.; Wang, K. X.; Liu, V.; Ma, Z.; Fan, S. Progress in 2D photonic crystal Fano resonance photonics. *Prog. Quant. Electron.* **2014**, *38*, 1–74.
- (45) Moumen, S.; Raible, I.; Krauß, A.; Wöllenstein, J. Infrared investigation of CO<sub>2</sub> sorption by amine based materials for the development of a NDIR CO<sub>2</sub> sensor. *Sens. Actuators, B* **2016**, *236*, 1083–1090.
- (46) Bernard, S.; Reinhardt, C.; Dumont, V.; Peter, Y.-A.; Sankey, J. C. Precision resonance tuning and design of SiN photonic crystal reflectors. *Opt. Lett.* **2016**, *41*, S624–S627.
- (47) Gao, X.; Hsu, C. W.; Zhen, B.; Lin, X.; Joannopoulos, J. D.; Soljačić, M.; Chen, H. Formation mechanism of guided resonances and bound states in the continuum in photonic crystal slabs. *Sci. Rep.* **2016**, *6*, 31908.
- (48) Qiang, Z.; Yang, H.; Chen, L.; Pang, H.; Ma, Z.; Zhou, W. Fano filters based on transferred silicon nanomembranes on plastic substrates. *Appl. Phys. Lett.* **2008**, *93*, 061106.
- (49) Chadha, A. S.; Zhao, D.; Chuwongin, S.; Ma, Z.; Zhou, W. Polarization- and angle-dependent characteristics in two dimensional photonic crystal membrane reflectors. *Appl. Phys. Lett.* **2013**, *103*, 211107.